npj | computational materials

Article

Published in partnership with the Shanghai Institute of Ceramics of the Chinese Academy of Sciences

https://doi.org/10.1038/s41524-025-01847-4

Demystifying local polarization configuration evolution for high-piezoelectricity chemical design via deep learning

Xingshuai Ma[1], Jian Fu[2], Longlong Fan[3], Jie Wu[4], He Qi[4] ✉, Shi Liu[5,6] ✉ & Jun Chen[1,7] ✉

Development of piezoelectric materials through chemical design meets the requirement of the next-generation electronic devices, yet the sensitive piezoelectricity to both chemical components and operational environment call for the trial and error method during material preparation. In order to give an atomic-level understanding about functional unit and assist the chemical design, deep learning was applied to train a novel model based on the most popular $BaTiO_3$ system, as a case study in this work. Through training the atomic force field of calcium and stannum doped solid-solution with Deep Potential method, 3D structure of chemical distribution and corresponding polarization configuration can be constructed for different compositions under different temperatures, which exhibits a high degree of consistency with the local structure quantitatively analyzed from HAADF STEM and reverse Monte Carlo refinement of neutron total scattering data, especially for the critical composition with ultrahigh piezoelectricity of d_{33} ~ 860 pC/N. Systemic analysis reveals that variations in chemical bond length among various elements with oxygen elements are the primary factors influencing ferroelectric activity and leading to structural evolution. The results and methodology can facilitate the discovery of new ferroelectrics and the design of high-performance piezo/ferroelectrics with atomic-level insights.

Ferroelectric perovskite materials possess fundamental applications in the field of electronic sensors, medical ultrasonic transducers, energy storage, etc.[1–3]. Phase boundary design has been attributed to be the most useful method to improve electrical performance. Take the most classic lead-based binary component Pb(Zr,Ti)O_3 (PZT) as an example, the optimal piezoelectric performance only appears at a narrow composition range around $Pb(Zr_{0.52}Ti_{0.48})O_3$, accounting for less than 1% of total[4,5]. In lead-free systems, such as (Na,K)NbO_3 and $BaTiO_3$ (BT), the flexible phase boundaries depend on not solely composition but also temperature comparing with the PZT. Furthermore, despite being located at the same phase boundaries, the disparity in their local polarization configurations converts corresponding properties significantly among different compositions, therefore complicating the material design and resulting in the extensive trial and error[3,6,7]. Hence, there is an urgent need to develop the guiding methodologies of phase boundaries and in-depth local polarization configuration design to accelerate the development of piezo/ferroelectric perovskite solid solutions.

Various theoretical calculation methods have been employed to elucidate the properties of ferroelectrics and the factors influencing ferroelectricity. At the microscopic scale, density functional theory (DFT) calculations have significantly advanced the understanding of the electronic structure, phonon dynamics, and phase stability in ferroelectric materials[8,9]. For instance, Yoshida et al. leveraged the second-order Jahn-Teller (SOJT) effect to delineate the requisite conditions for the formation of the torsional mode (non-zone-center phonons) by considering electro-acoustic coupling[10]. Meanwhile Gu et al. proposed a mechanism that enhances the ferroelectric by the coupling between the torsional and ferroelectric modes[11].

---

[1]Department of Physical Chemistry, Beijing Advanced Innovation Center for Materials Genome Engineering, University of Science and Technology Beijing, Beijing, China. [2]Institute of Electro Ceramics & Devices, School of Materials Science and Engineering, Hefei University of Technology, Hefei, China. [3]Institute of High Energy Physics, Chinese Academy of Sciences, Beijing, China. [4]School of Materials Science and Engineering, Hainan University, Haikou, Hainan Province, China. [5]Key Laboratory for Quantum Materials of Zhejiang Province, Department of Physics, School of Science, Westlake University, Hangzhou, Zhejiang, China. [6]Institute of Natural Sciences, Westlake Institute for Advanced Study, Hangzhou, Zhejiang, China. [7]State Key Laboratory of Tropic Ocean Engineering Materials and Materials Evaluation, Hainan University, Haikou, China. ✉e-mail: qihe@hainanu.edu.cn; liushi@westlake.edu.cn; junchen@ustb.edu.cn

Kim et al. systematically investigated the phonon behavior of $NaNbO_3$ and $KNbO_3$ at finite temperatures, and by incorporating bubble self-energies, they obtained phase transition temperatures and dielectric constants that closely match experimental data[12]. Phase field simulations, through the evolution of Landau free energy under varying conditions, have provided insights into the polarization distribution in ferroelectrics. By establishing a coupling between polarization and energy, these simulations offer a mesoscale understanding of ferroelectric behavior[13,14]. For instance, the origin of the high-piezoelectric relaxor ferroelectrics, specifically the function of polar nano-micro regions and their "transverse instability" phenomenon[15–17]; the function of multi-scale control techniques to the switching of ferroelectric heterostructures between topological, spiral, ferroelectric, antiferroelectric, and paraelectric states from simulation level[18–21]; the impact of vacancies and dislocations to the evolution of ferroelectricity[22,23]. Although current theoretical models have addressed numerous aspects of ferroelectric phenomena successfully, some blank region still remains between the microscopic and mesoscopic scales, specifically in terms of establishing a direct relationship between polarization evolution and atomic-level structural configurations.

With the rapid development of deep learning based on Artificial Neural Networks (ANNs), it has been widely applied across various fields, particularly making a significant impact in materials science[24,25]. One of the key methods, Deep-learning Potential (DP), offers a promising solution to fill the vacancy[26,27]. For DP, it constructs a training set leveraging DFT calculations, where atomic coordinates and types are used as input layers, and energy serves as the output layer for the ANN model. Any well-trained DP model can predict the influence of atomic position changes on energy with DFT accuracy[26,27]. Therefore, it provides a bridge between the point-to-point atomistic behavior and energy evolution, allowing the system's characteristics to be described through molecular dynamics (MD) simulations without relying on any external parameters. Despite the limited interpretability of neural network algorithms[28], which hinders the understanding of the underlying physical mechanisms of materials, such as DP possesses the ability to only describe potential energy and kinetic energy, and its inability to visualize the variations of concrete energy such as gradient energy or strain energy as done by phase-field methods, or the evolution of electrons before and after the structural changes as done by DFT calculations—DP, as an emerging approach, has still made some meaningful progress in several fields such as surface dynamics[29], phase diagrams[30,31], two-dimensional materials[32–35], and thermal behavior[36–38], etc.

For this work, in order to deeply understand the origin of high piezoelectricity caused at atom scale and accelerate the chemical design, DP is primarily applied to construct the novel perspective in conjunction with DFT calculations to further clarify the mechanism, as taking the most popular lead-free piezoelectric system $BaTiO_3$ to be the case[39]. After the realization of high $d_{33} \sim 620$ pC/N in $Ba(Ti_{0.8}Zr_{0.2})O_3$-x$(Ba_{0.7}Ca_{0.3})TiO_3$ system by Liu et al.[4], numerous experiments have been reported for enhancing piezoelectric performance by introducing of appropriate elements such as Ca and Sr to the A-site, and Sn, Hf, and Zr to the B-site in $BaTiO_3$. Yet few works with better piezoelectric performance have been reported in (Ba,Ca)(Ti,Zr)O_3 system in the past decade. Differently, based on the similar conception of phase boundary construction, higher $d_{33} > 700$ pC/N can be achieved by Sn instead of Zr[40,41]. Especially, our previous research results indicate that a high $d_{33} \sim 860$ pC/N can be detected in $Ba_{1\text{-}y}Ca_yTi_{1\text{-}x}Sn_xO_3$ when fix the Ca and Sn content around 0.075 and 0.1[42]. Therefore, not only the average phase structure evolution, but also the effect of each element on the local polarization configuration should be studied in detail. In this work, with the help of DP, solid solution model for $Ba_{1\text{-}y}Ca_yTi_{1\text{-}x}Sn_xO_3$ ($0 \le x \le 0.25$, $0 \le y \le 0.25$) was successfully established. With the predicted capacity of DP model, only several discrete components are sufficient to reflect the continuous change of composition when the datasets of the above discrete models are combined into one. At the same time, the detailed local chemical distribution and polar vectors were quantitatively analyzed in terms of high-angle annular dark field (HAADF) scanning transmission electron microscopy (STEM) and reverse Monte Carlo (RMC) refinement on neutron-based pair distribution function (PDF), which are used to verify rationality of the predicted mapping from the DP models.

Results

The construction and performance of DP models

As the temperature increases, the ferroelectric morphology of pure $BaTiO_3$ undergoes a phase transition sequence from rhombohedral (*R3m*) to orthorhombic (*Amm2*), tetragonal (*P4mm*), and finally cubic ($Pm\bar{3}m$). This transition is characterized by polarization along the [111], [110], and [100] directions, respectively. The Polycrystalline Phase Transition (PPT) represents a dynamic process that is typically influenced by doping engineering, making the DP method the most suitable research approach. Due to the complexity of element types and their atomic occupancy, investigating the dynamic evolution in solid solutions is hindered by the vast number of structures within the parameter space. However, leveraging the learning and fitting capabilities of deep neural networks, only a relatively small and discrete training set, uniform in parameter space, can adequately describe the expansive and continuous sample space. Thousands, or even hundreds, of DFT frames can be used to construct a suitable DP model that approximates DFT calculations with reasonable accuracy. In this study, a joint doping system of tantalum and calcium with eleven frames were chosen to construct $Ba_{1\text{-}y}Ca_yTi_{1\text{-}x}Sn_xO_3$ ($0 \le x \le 0.25$, $0 \le y \le 0.25$) solid solution potentials (Fig. 1e). The process can be divided into four steps: model training, sample space exploration, convergence judgment (labeling) and data-set making in Fig. 1a-d. The model training step (Fig. 1a) aims to utilize the atomic coordinates from DFT calculation as the initial input set, with corresponding energy as the target to construct four DP models with the same descriptor (or training set) with various initial parameters. In the sample space exploration step (Fig. 1b), leveraging MD simulation to explore the parameter space at different temperature with a certain model mentioned above, a large number of random structures will be obtained subsequently. The structures are divided into three categories according to the average error (named Δ) to corresponding structures about the models mentioned above, counting for the "Accurate" ($\triangle < \sigma_{low}$), "Candidate" ($\sigma_{low} < \triangle < \sigma_{high}$) and "failure" ($\sigma_{high} < \triangle$) in labeling process (Fig. 1d). Randomly choose several frames within "Candidate" sets to execute DFT calculation and combine their results into training-set (Fig. 1c). Repeat the iterations until the models reveal nearly consistent to random structures, regarding as convergence. Figure. S1 compares the DFT and DP results for random structures in terms of energy and interatomic forces. Both distributions exhibit nearly linear patterns, leading to favorable evaluation indicators (RMSE, MAE, and R^2) and lower error dispersion (see Fig. S1 insets). Additionally, the complete agreement of the phonon dispersion spectrum in Fig. S2 demonstrates the ability of DP models to accurately describe interatomic behavior in three-dimensional space.

The influence of doping elements on average structure

Figure 2 presents the phase diagram derived from the modification of the normalized cell constant and lattice angle (Figs. S3–4) using the DP method, consistent with the behavior of PPT in lead-free perovskite ferroelectrics[3,6,7]. In the case of low-concentration doping, the contrasting effects of stannum and calcium doping on the Curie temperature necessitate careful consideration, as these elements are generally classified as non-ferroelectric (as discussed further below). For ferroelectrics, the defining characteristic is the ionic displacement of cations relative to anions, which can be quantified as

$$\vec{d}_i = \vec{x}_i - \frac{1}{n}\sum_{j}^{n} \vec{x}_{O_j} \tag{1}$$

For ABO_3 perovskite ferroelectrics, image a cation i locates in the polyhedron cage constructed by its adjacent oxygen, where the relative ionic displacement $\vec{d}_i$ could be defined as the difference between the coordinate of the cation $\vec{x}_i$ and the average coordinate of its neighbor oxygen $\vec{x}_{O_j}$, while n

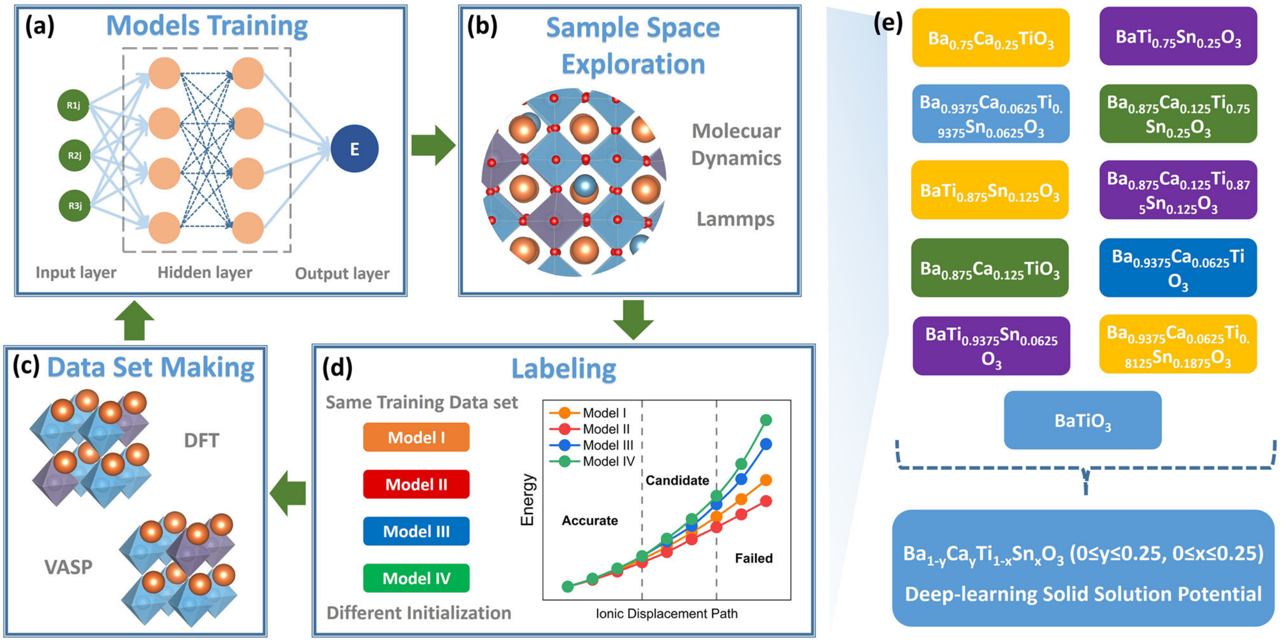

Fig. 1 | The flowchart of training solid solution Deep-learning Potential (DP) model. The left (**a**–**d**) depict the general process of constructing any DP model, dividing into four steps: **a** models training, **b** sample space exploration, **c** data-set making and **d** labeling. The right (**e**) provides the constitution of $BaTiO_3$ based solid-solution potential in this work. Due to the inherent predictive ability of Artificial Neural Network, the continuous content of the solid solution can be decomposed into eleven discrete units as shown in the right region. For any discrete unit, it is necessary to repeat the left process until the DP models converge completely.

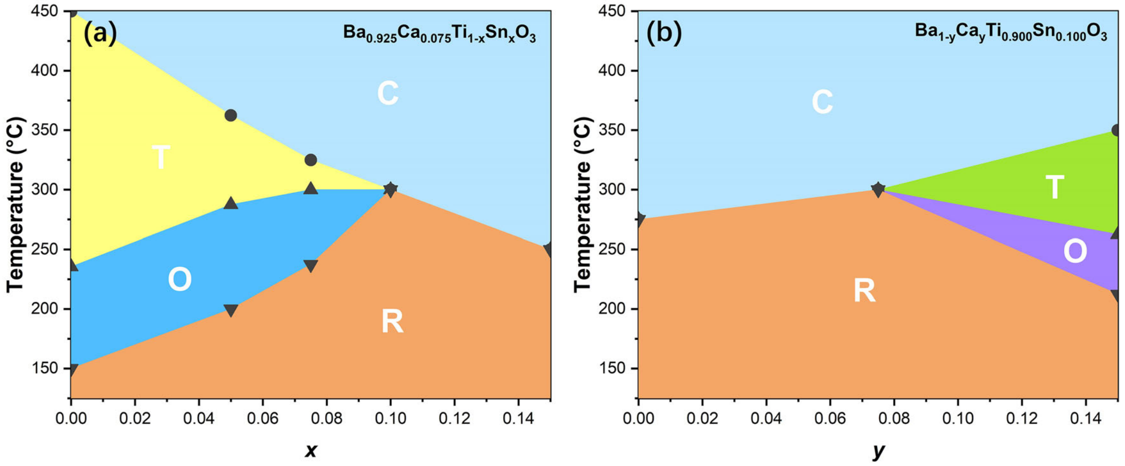

Fig. 2 | The phase diagram acquired by DP method. **a**, **b** depict the impact of Sn and Ca doping, respectively.

represents the coordination number, which is 12 and 6 for A and B cations, respectively. Thus, in three-dimension space the cation i possesses the displacement vector (d_{ix}, d_{iy}, d_{iz}). The average ionic displacement of a certain element can be obtained by taking the average of all the cations of this type. This can be expressed in the following formula:

$$\left(\bar{d}_x, \bar{d}_y, \bar{d}_z\right) = \left(\frac{1}{m}\sum_{i}^{m} d_{ix}, \frac{1}{m}\sum_{i}^{m} d_{iy}, \frac{1}{m}\sum_{i}^{m} d_{iz}\right) \tag{2}$$

Here, m denotes the number of cations i. And the Total Average Ionic Displacement (TAID) is the modulus of displacement vector defining as

$$\bar{d} = \sqrt{\bar{d}_x^2 + \bar{d}_y^2 + \bar{d}_z^2} \tag{3}$$

Typically, the structure and properties within the room temperature range are of significant interest. Figure 3 illustrates the variation in the normalized cell constant and TAID at 300 K as a function of doping concentration. Notably, Fig. 3b, d suggest that the magnitude of ionic displacement follows the order of Ca, Ti, Ba, Sn, indicating the great ferroelectric activity of Ca which breaks the situation that form the conventional understanding, researchers regard both Ca and Sn as non-ferroelectric activity ions. For Sn-doped specimens, as the doping concentration x increases, the c-axis gradually approaches the a (or b) axis, accompanied by a reduction in ionic displacement (Fig. 3b), signifying a weakening of tetragonality. An evident transition occurs near the critical composition, around $Ba_{0.925}Ca_{0.075}Ti_{0.9}Sn_{0.1}O_3$, where the material exhibits a pseudo-cubic phase, as shown in Fig. 3b. At this point, high piezoelectric performance is observed, consistent with extensive experimental findings. When it exceeds the edge, beyond the Curie Temperature brings the cubic phase that tends to ionic displacement fiercely collapse with steeper slope

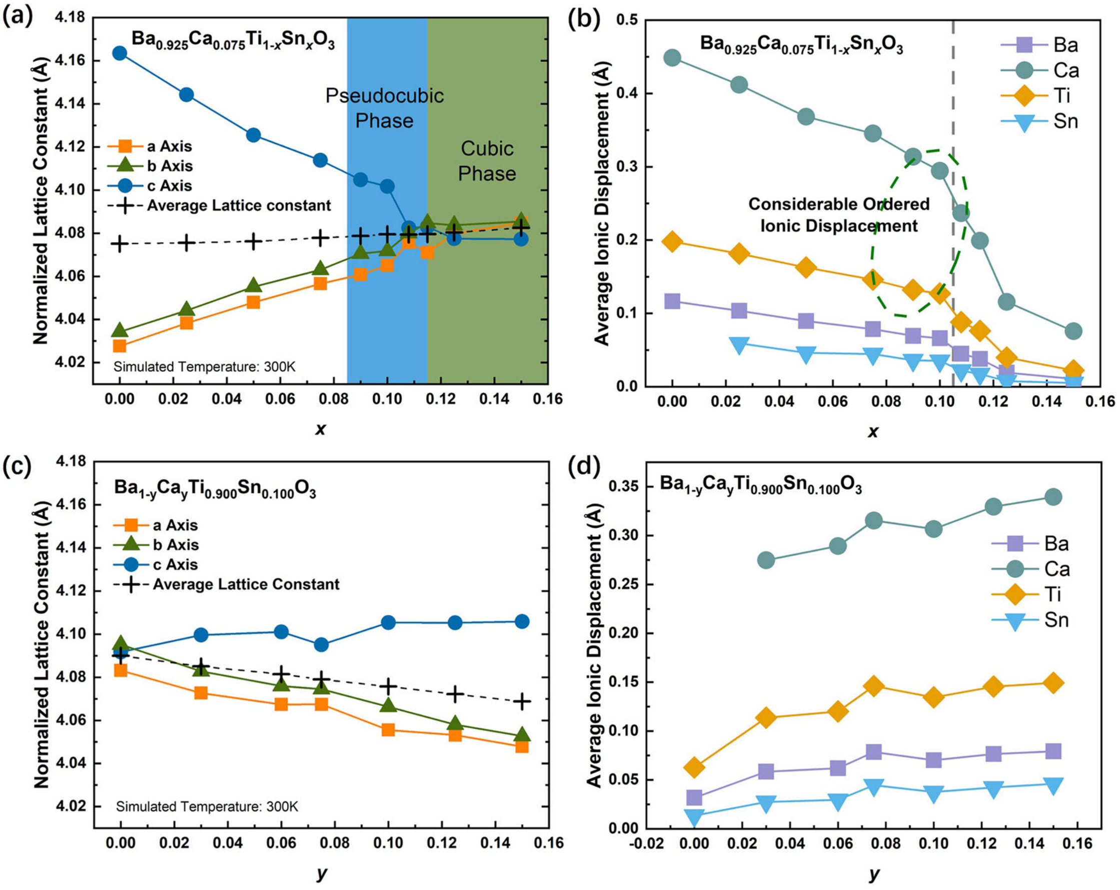

Fig. 3 | The normalized lattice constant and average ionic displacement (macroscopic residual ionic displacement). a, **b** The normalized lattice constant and its corresponding relative average ionic displacement of each cation: Ba^{2+}, Ca^{2+}, Ti^{4+} and Sn^{4+} within the component of $Ba_{0.925}Ca_{0.075}Ti_{1-x}Sn_xO_3$ versus the variation of Sn content at simulated temperature 300 K. **c**, **d** The normalized lattice constant and its corresponding relative average ionic displacement of A and B sites with the variation of Ca content in the component of $Ba_{1-y}Ca_yTi_{0.900}Sn_{0.100}O_3$ at 300 K.

distinguishing from before. In contrast, increasing the Ca content while fixing the Sn concentration enhances the TAID and regenerates the T-phase characteristics, as shown in Fig. 3c, d, conforms the result of the ferroelectric activity of Ca mentioned above.

The influence of doping elements on local polar configuration

Owing to the minimal distortion associated with the pseudo-cubic average phase structure in compositions containing a high concentration of foreign atoms, particularly following the emergence of relaxor behavior, it is crucial to examine the local symmetry in greater detail. Figure 4 and S6 illustrates the evolution of cation distribution and the corresponding polarization vector configuration in random atomic layer at a simulated temperature of 300 K. When the Ca content is fixed, as shown in Fig. 4a–c, it is evident that the vector distribution at the B site becomes increasingly disordered upon the introduction of Sn, resulting in a transition from a T-phase dominated structure to a mixed R-O-T multiphase. At $x = 0.1$, slush-like polar clusters, separated by high-density, low-symmetry domain walls, are observed in Fig. 4c, h, resembling the unique structure reported in PMN-PT and KNN-based ceramics with high piezoelectric properties[43,44]. Furthermore, the ionic displacement distribution of this slush-like configuration is not static but exhibits dynamic fluctuations over time[45,46]. With further introduction of Sn, the phase energies of R, O, T, and C begin to approach each other, resulting in the appearance of a localized cubic paraelectric matrix with isolated polar nanoclusters, as shown in Fig. 4d–f. At this point, the system has basically entered a relaxation state[47,48].

Different from the effect of Sn, it is evident that Ca exhibits a relatively large displacement, as depicted in Fig. 4g–i, conforms to the behavior in Fig. 3. Maintaining constant Sn content, an increase in Ca content effectively rescues the fading cation displacement from a weak relaxation state to a multi-phase coexisting state, as illustrated in Fig. S6. In comparison to Sn doping, Ca offers the opposite and relatively inconspicuous functionality, where a considerable amount of substitution could solely optimize the structural configuration to a certain extent. Additionally, Ca doping attenuates polar magnitude and gradually reduces the chemical bond of Ti-O caused by lattice shrinkage (further details will be elaborated below), thereby adversely impacting all polarization-related properties. Consequently, fine control over phase boundaries represents the primary application of Ca doping.

Based on the 3D atomic configuration obtained from MD, we extracted the position information of oxygen ions coordinated with their nearest neighbors for each element. Figure 5a, b illustrates the radial distribution function (RDF), representing the probability density of other elements appearing around a certain referential oxygen. If a certain type of element exhibits stronger ferroelectric activity, it will tend to form closer hybridization with one type of oxygen ions, resulting in greater off-centering displacement. This is reflected in the discreteness of the three bonds mentioned above and aligns with the RDF distribution of Ti and Ca. On the other hand, Sn and Ba exhibit opposite behavior, especially evident in the sharp RDF peaks of Sn indicating its stability inside the cell without significant differences among the three bonds. Figure 5c–f illustrates the correlation between the three bond lengths formed by Ba, Ca, Ti, and Sn ions with the adjacent oxygen and their average as a function of Sn doping content. It is observed that under the same x, the degree of separation in the three types of bonds follows a descending order of Ca, Ti, Ba, and Sn, consistent with the variation pattern of RDF mentioned earlier. It is noted that the splitting amplitude of these bonds

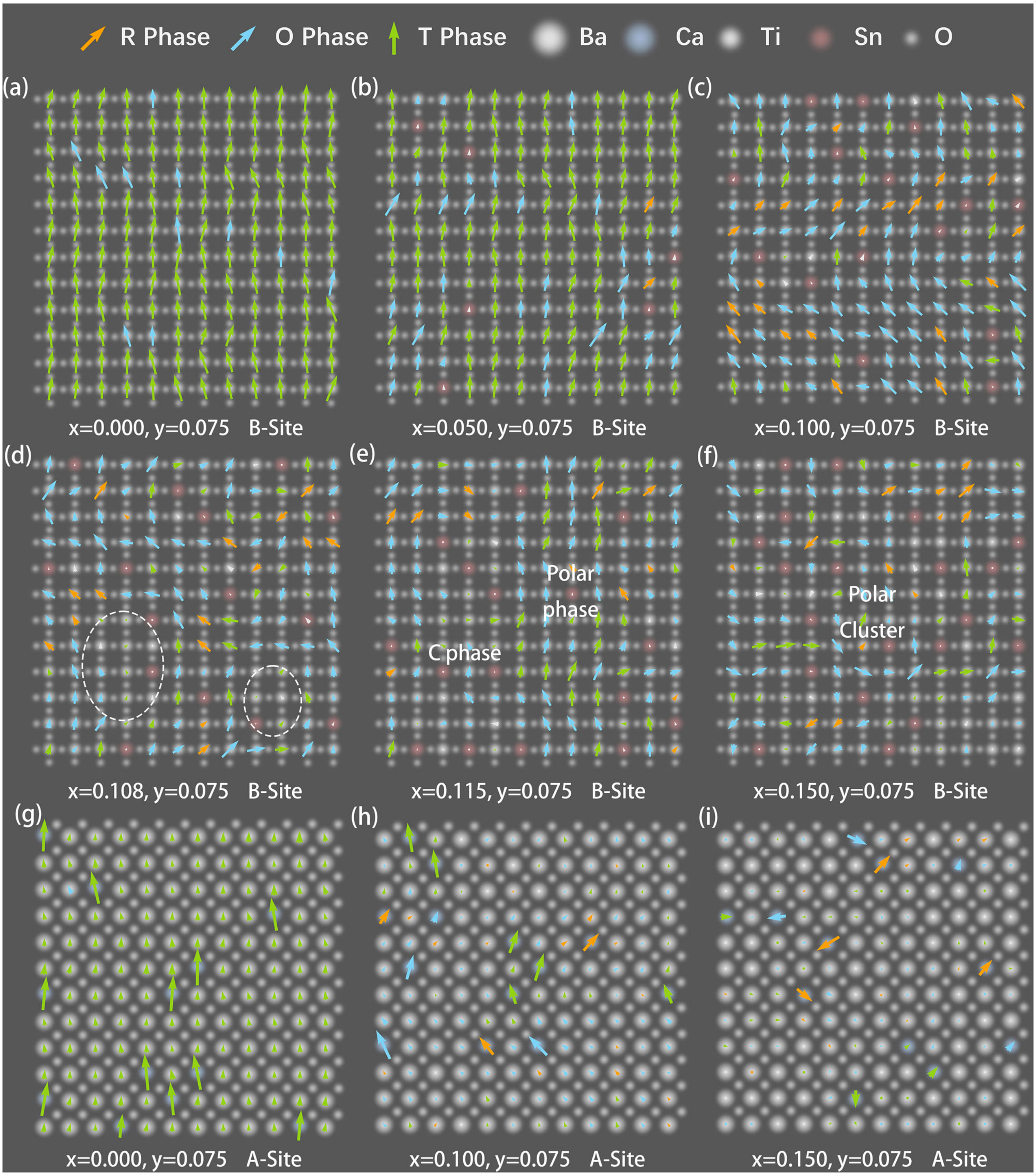

Fig. 4 | Local ionic displacement distribution of the random selected atomic layer of $Ba_{1-y}Ca_yTi_{1-x}Sn_xO_3$ with Sn doping content change at 300 K from the DP result. Orange, Blue and green arrows respectively represent Rhombohedral (R), Orthorhombic (O) and Tetragonal (T) phases. The larger bule and smaller red dots represent A-site doped Ca ions and B-site doped Sn ions, while the gray dots arranged from large to small represent Ba, Ti and O, respectively. Fixing the Ca content y as 0.075 while converting the Sn content as 0.000, 0.050, 0.100, 0.108, 0.115 and 0.150, respectively, **a**–**f** depict the mapping of structure evolution at the B-site from almost single phase gradually to coexistent phase, finally to relaxed phase, implying the attenuation of ferroelectric activity with Sn introduction. **g**–**i** paint the several corresponding A-site situations, indicating the import of Ca ions bring extra ferroelectric activity in the premise of following the tendency of structure variation.

decreases with increasing Sn content, indicating a convergence of element positions towards the average coordinates of the oxygen polyhedral cage and a weakening of ferroelectricity. The intrinsic symmetry changes gradually from a highly ordered T phase to locally disordered multiphase, as can be directly reflected on the stereographic projection in Fig. 5g (more details refer to Figs. S8–10).

Additionally, it is counterintuitive that the average Ti-O bond length decreases with the enhancement of Sn doping (Fig. 5e, from ~2.04 Å to ~2.03 Å, the corresponding slope: −0.0618), despite Sn^{4+} having a larger ionic radius than Ti^{4+} (see Fig. 3a, where the average lattice constant expands with positive slope: +0.0483), indicating a significant localized compressive stress on Ti-O bonds. On the contrary, Ca^{2+} possesses smaller character that

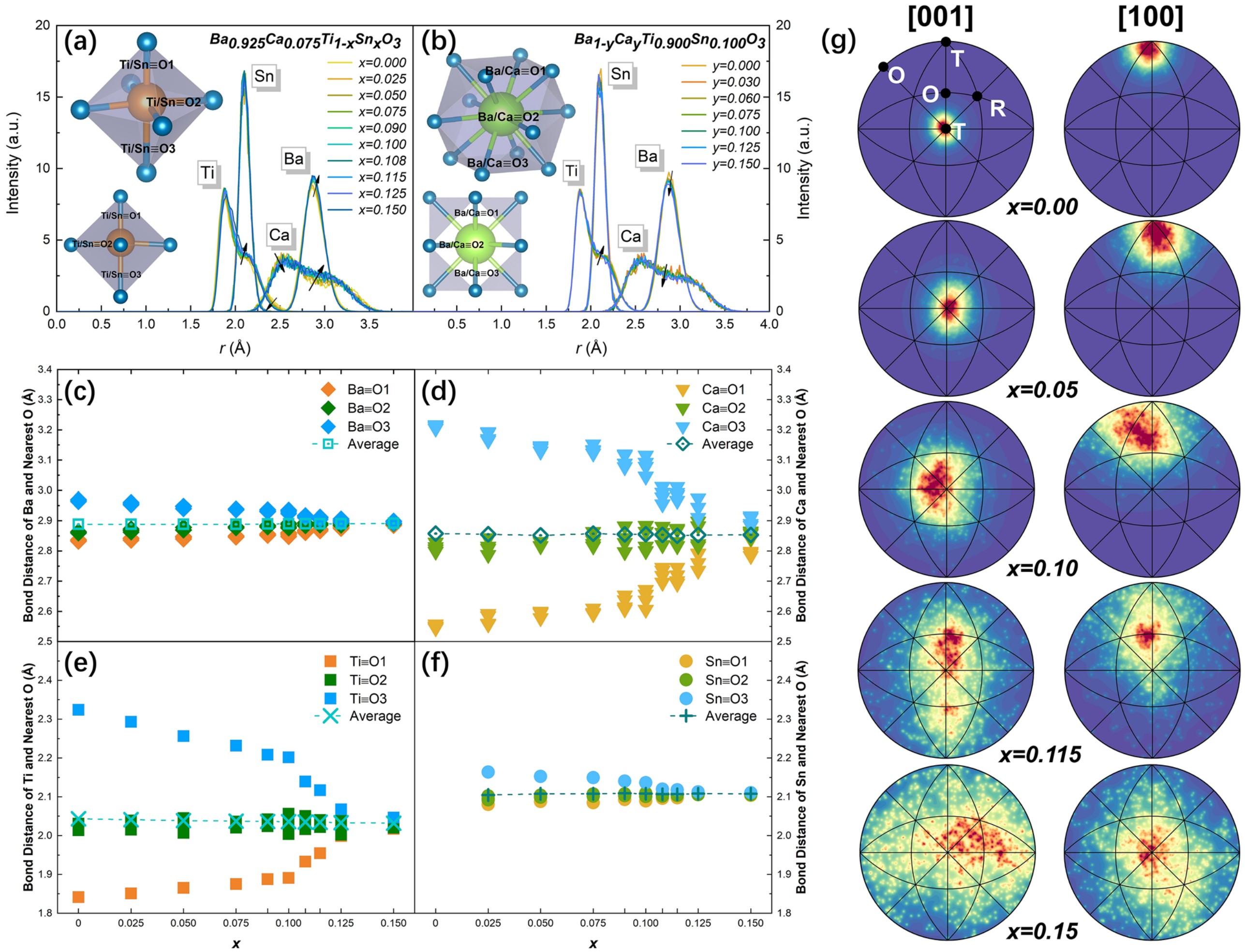

Fig. 5 | The radial distribution function (RDF) and nonequivalent bond length. **a**, **b** The radial distribution function (RDF) of related elements through altering Sn and Ca content, respectively, where the black arrow represents the trend of RDF shape change with increasing doping amount. For ABO_3 type ferroelectric materials, the inset displays polyhedral cages formed by A and B-sites and their adjacent coordinating oxygens, as well as three different types of bonds. **c**–**f** The relationship between the three types bond of Ba, Ca, Ti and Sn cations with their adjacent oxygens and corresponding average values depending on Sn content variation. **g** Stereographic projection viewing of the displacements along [001] and [100] directions counting all cations. All the above results are extracted from the 3D atomic configuration of molecular dynamics simulation applying the DP model.

Ba^{2+} (~1.340–1.610 Å with 12-coordination, according to Shannon radii), however remains much gently slope of Ti-O altering (see Fig. S7c, the corresponding slope: −0.0618) compared to the variation of lattice constant (see Fig. 3c, the corresponding slope: −0.1398), revealing the localized tensile stress on Ti-O bonds.

Mechanism understanding

The effects of different doping elements on macroscopic properties and local structures are revealed by DP, while further understanding their influence mechanisms remains crucial for material design. As early as 1990, Cohen et al. conducted an investigation into the relationship between polar direction and energy variation of $BaTiO_3$ at different volumes utilizing the DFT method[49,50]. Their work illustrates the significant dependence of $BaTiO_3$ free energy on volume (or bond length) variation. This finding may offer a plausible explanation for the doping effect. Under a cubic cell ($a = b = c$) with lattice constants respectively as 4.07 Å, 4.02 Å and 3.97 Å, the relative energy of R, T, and C phases gradually evolves within their potential-wells as depicted in the Fig. 6a. With decreasing lattice constant to 4.02 Å, the energy valleys of both R and T phases begin to approach each other. This result in line with macroscopic multiphase coexistence morphology with stable polarization in Fig. 4c. Upon reaching a lattice constant of 3.97 Å, where the corresponding Ti-O bond length is ~1.985 Å nearly approaching $SrTiO_3$ with *I4/mcm* and $Pm\bar{3}m$ phases (listed in Table S1), it becomes evident that energies of R, T and C phases tend to converge towards consistency, revealing the flat energy barrier within each phase. At this point, due to dynamic fluctuations in polarization leading to alternating appearance and annihilation of C phase, as well as polar directions converting to their equivalent directions repeatedly, macroscopic ferroelectricity disappears (Fig. 4e). In conclusion, for B-site driven ferroelectric material $BaTiO_3$, a decrease in Ti-O bond accelerates the evolution of each ferroelectric states and reduction in ferroelectric activity.

With the introduction of Sn doping, the compressive stress leads to a significant decrease in the local neighboring Ti-O bonds, resulting in the phenomenon from above viewpoint. This ultimately causes a decrease in the Curie Temperature and induces phase configuration conversion. In contrast to Sn doping, Ca^{2+} doping exerts an opposing effect due to the tensile stress on neighboring Ti octahedral cages, resulting in the enlargement of local Ti-O bonds and inducing additional ferroelectric activity. However, this mechanism for enhancing polarization is not sustainable, as the smaller ionic radii of Ca^{2+} lead to a decrease in average lattice constant and average Ti-O bond length (Fig. 3c and S7c). The polarization will diminish when the average Ti-O bond approaches a certain value, perhaps ~2.016 Å similar to the C phase ($Pm\bar{3}m$) in $BaTiO_3$ (Table S1). Therefore, the influence of Ca doping to the Ti-O bond can be characterized by a competitive relationship between enhanced localized ferroelectricity due to local tensile stress and decreased overall ferroelectricity due to a reduction in average Ti-O bond. Furthermore, it is evident that Ca^{2+}

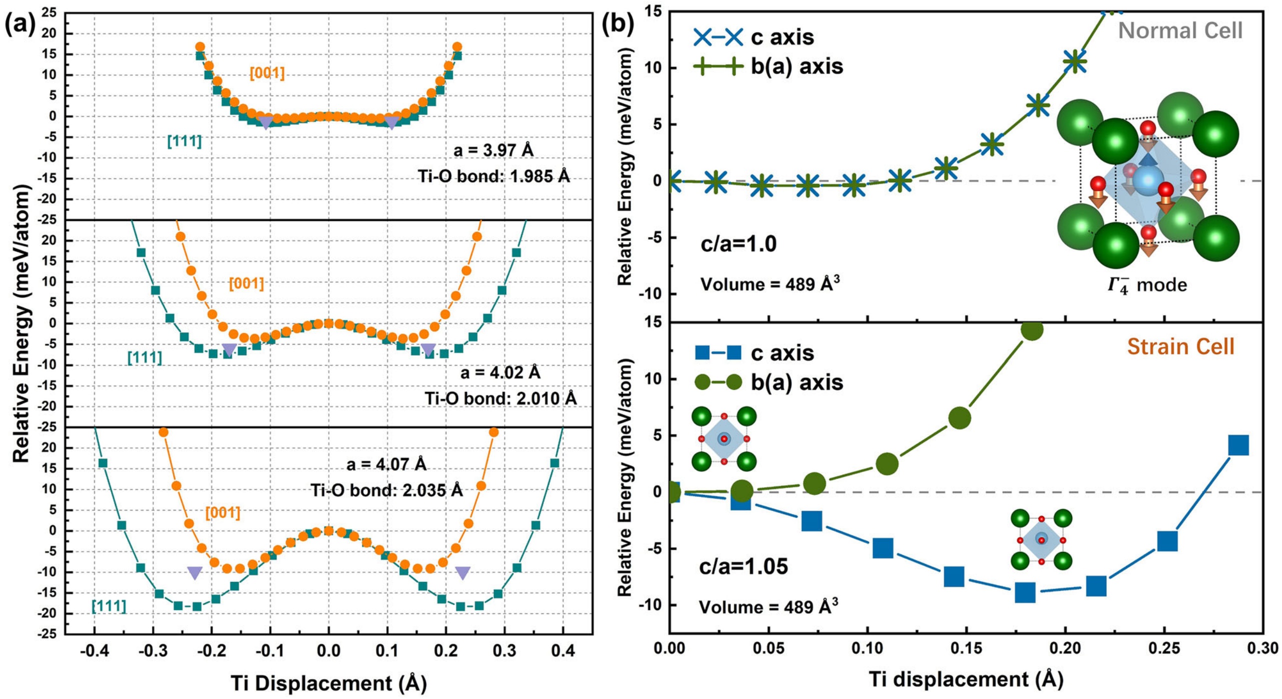

Fig. 6 | The illustration of "bond-length" effect to ferroelectric activity. a The relative energy well and barrier of pure $BaTiO_3$, with respect to Ti ionic displacement under the cubic structure ($a = b = c$) with various volumes, were calculated utilizing the DFT method with a $2 \times 2 \times 2$ supercell, where Calculations were performed along the [111] direction (R phase, represented by the bottle-green curve) and the [001] direction (T phase, represented by the orange curve). The purple triangle represents the most stable T-phase structure after introducing tetragonal distortion ($a = b < c$) and its corresponding energy. The paraelectric phase locates Ti displacement value as zero. **b** The relative energy of $SrTiO_3$ with constant volume in a $2 \times 2 \times 2$ supercell was calculated for both the cubic cell ($c/a = 1.0$, $a = b = c$) and the strained cell ($c/a = 1.05$, $a = b < c$), with respect to Ti displacement along the Γ_4^- vibrational mode in each nonequivalent direction. The Ti displacement locates at zero measures the non-polarized phase.

exhibits significant off-centering displacement even larger than Ti, contrary to the common perception that Ca^{2+} lacks ferroelectricity, which can be attributed to the "bond-length" perspective as well.

The method of inducing ferroelectricity through largening bond lengths is not solely a volume effect, in fact, only a specific direction is still able to produces substantial bond length effect. Taking $SrTiO_3$ as an example, as an incipient ferroelectric, no macroscopic ferroelectric activity can be observed even at 0 K[51–54]. However, abundant theoretical and experimental evidence that macroscopic ferroelectricity can be triggered in $SrTiO_3$ through epitaxial strain[55,56]. The phonon spectrum calculation results from DFT show that significant imaginary frequencies are mainly located at the Gamma in the center of the Brillouin region and R points in the cubic phase ($Pm\bar{3}m$) of $SrTiO_3$[57,58]. The mode corresponding to the imaginary frequency at point Gamma is identified as Γ_4^- optical mode. It is evident that softening of Γ_4^- mode signifies the generation of ferroelectricity. Figure 6b employs the DFT method to calculate the relative energy of $SrTiO_3$ in a $2 \times 2 \times 2$ supercell, depicting both the normal cubic cell ($c/a = 1.0$, $a = b = c$) and the strain cell ($c/a = 1.05$, $a = b < c$) versus Ti displacement along the ferroelectric Γ_4^- mode in each nonequivalent direction. In the cubic cell, the Ti-O bond length (Table S3) along three directions are equivalent to 1.970 Å, referred as a quantum paraelectric material[59,60]. Upon application of the strain ($c/a = 1.05$), it is observed that the length of the Ti-O bond increases to 2.035 Å along c axis. Evidently, there is a lower potential energy curve along the c direction compared with paraelectric phase, indicating emergence of a stable ferroelectric phase along this axis. Simultaneously, the reduction in bond length to 1.938 Å along b axis results in a steeper potential energy surface, hindering the generation of polarization. Despite only one direction meeting requirements for "bond length" effect for the generation of ferroelectric activity, macroscopic polarization can still ensue.

From a deeper microscopic perspective, particularly at the level of electronic interactions, the ferroelectricity of materials which exhibit the polyhedral characteristics primarily results from the competition of the covalent bonds formation (leading to the ferroelectric phase and lower the energy) and Coulomb repulsive interactions (leading to the paraelectric phase and increase the energy)[61,62]. The increase in bond length facilitates the reduction of Coulomb repulsion energy, thereby stabilizing the ferroelectric phase. As early as 2009, Rondinelli et al. predicted that by increasing the bond length, $BaMnO_3$ would more readily stabilize the ferroelectric phase compared to $CaMnO_3$, a prediction subsequently confirmed in later experimental studies[62,63]. The fundamental physical mechanism underlying these phenomena can be attributed to the SOJT effect (details can be found in the Supplementary materials)[64–66]. Thus, through judicious chemical bonding (or crystal structure) design, it is possible to systematically manipulate and control ferroelectricity, even inducing ferroelectric behavior in materials such as $BaSnO_3$, which is conventionally considered a paraelectric phase (refer to Fig. S16). Therefore, the strategic selection of cations and their coordination environment (usually referring to the point group of polyhedral cages) is key to the development of novel ferroelectric materials.

Experimental verification

The experimental results indicate that large d_{33} reaches up to 860 pC/N can be measured in the composition approaching to $Ba_{0.925}Ca_{0.075}Ti_{0.9}Sn_{0.1}O_3$, which is chosen as the case to deeply reveal the real structure in detail. At microscale, slender domains embedded in nanodomains with weak contrast can be in the bright-field TEM along [001] in Fig. 7. Due to the fact that absence of oxygen in HAADF STEM images, the ionic displacement is measured by the shift of A (B) to the average center of neighboring B (A) atoms. Then the relationship between the vector direction with the corresponding ferroelectric phase is given in Fig. 7c, that T phase is along [100] and R/O phases are parallel to [110] with four equivalent directions in 2D plane. Similar to the polarization mapping obtained from DP method (Fig. 7d), hetero-structure slush-like clusters with multiphases are separated

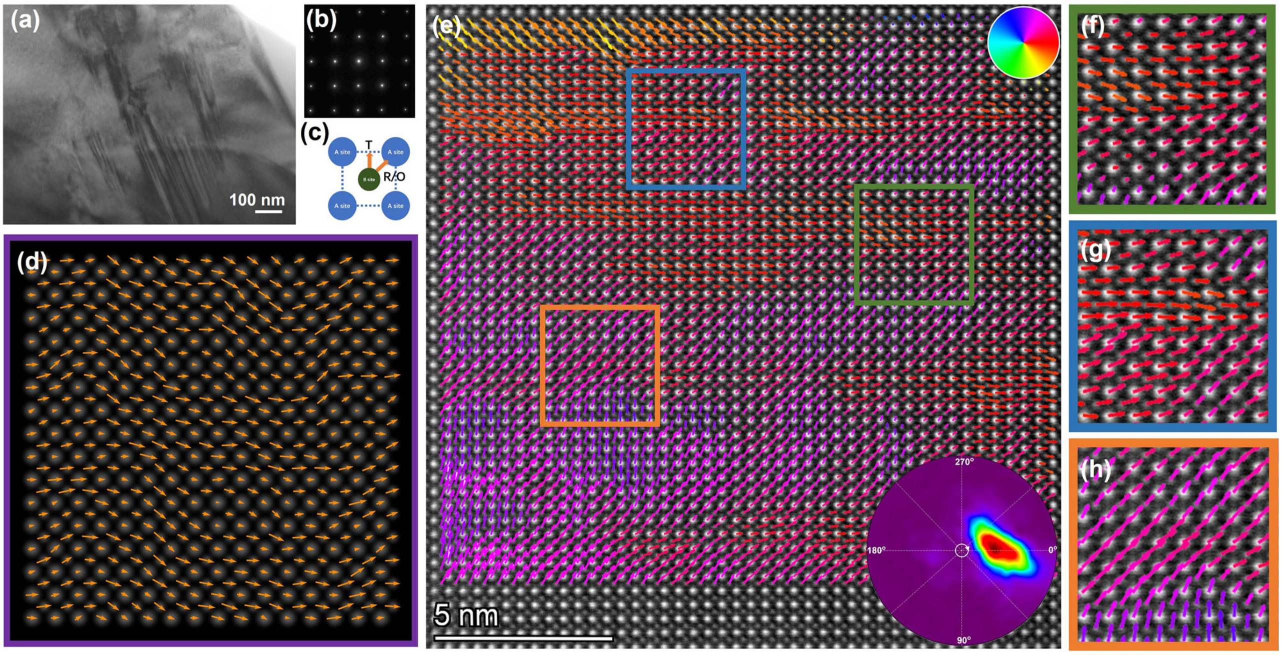

Fig. 7 | The comparison of mappings of polar distribution between DP model and experimental result. **a** Bright-field TEM image, **b**, **c** selected area electron diffraction and ionic displacement calculation method in 2D plane for the ceramic of $Ba_{0.926}Ca_{0.074}Ti_{0.892}Sn_{0.108}O_3$. **d** Polarization mapping obtained from DP for the composition of $Ba_{0.925}Ca_{0.075}Ti_{0.9}Sn_{0.1}O_3$. **e** Polarization mapping on the STEM image and corresponding polarization vector distribution. **f**–**h** local magnification in STEM mapping for the ceramic of $Ba_{0.926}Ca_{0.074}Ti_{0.892}Sn_{0.108}O_3$.

by low-symmetry domain walls can be found for the polarization mapping on HAADF STEM (Fig. 7e). The locally enlarged images in Fig. 7f–h further clearly show the polar nanoregions with R, O, T, and even monoclinic (M) phases, indicating that their energies are close to each other without obvious energy barriers. Compared to the random and disordered polar distribution of traditional relaxor ferroelectrics with strong ergodicity, the polar vectors in this studied sample still have a preferred orientation at microscopic scale, that ensures the excellent piezoelectric property.

The atomic pair-distribution function (PDF) technique based on neutron total scattering together with big-box modeling by a Reverse Monte Carlo (RMC) algorithm is used to reveal the 3D chemical distribution as well as the corresponding ferro-distortion (Fig. 8). The fluctuation of polarization angles and polarization magnitudes leads to the obvious nanoclusters (Fig. 8b, c), simultaneously, stereographic projection reveals the fluctuation of polar symmetries with the coexistence of R-O-T and their intermediate M phases (Fig. 8d, e). The statistical results for the average off-centering cation displacement also exhibit a good consistency with the DP calculated results, that the small-size Ca exhibits a relatively large displacement in consistent with previous work[67], the non-ferroactive Sn has little displacement (Fig. 8f), contributing to the additional ferroelectricity and the destruction of the long-range ordered polarization, respectively.

The local polar heterogeneity should be mainly related to the local chemical inhomogeneity (Fig. 8g, h). Firstly, the Ca tends to move to a corner even though it has a strong polarization. Secondly, the introduction of nonpolar sites on Sn not only breaks the polarization ordering but also introduces the local random stress field, allowing the appearance of different symmetries in each nanocluster along with decreasing the free energy barriers between them. Lastly, the local random stress field caused by the substitution of equivalence alien atoms affects the chemical order regions composed of Ba and Ti, leading to the obviously decreased displacement magnitude by comparing with that of $BaTiO_3$.

Discussion

In summary, we employed deep learning techniques to establish the interatomic potential of calcium and stannum doped $BaTiO_3$ complex solid solution, elucidating the impact of dopant elements on their ionic displacement and lattice, as well as their role in local atomic configuration evolution. The findings suggest that stannum doping suppresses long-range ordered ferroelectricity, resulting in a transition from a single and ordered ferroelectric state to a multiphase state, eventually leading to a relaxor ferroelectric state. In contrast, low concentrations of calcium doping slightly enhance ferroelectricity, opposite to the effect of stannum. The "bond length" effect is proposed to explain this phenomenon - that an increase in bond length favors the stability of a single-phase ferroelectric state, which is further validated through DFT calculations on pure $BaTiO_3$, $SrTiO_3$, and $BaSnO_3$. Large-scale MD simulations show that the relatively large and small ionic radii of Sn^{4+} and Ca^{2+} introduce compressive and tensile stresses, respectively, altering the patterns of neighboring Ti-O bonds and thus driving the evolution of the ferroelectric phase. The polarization configurations built from experimental data show good agreement with those predicted by the DP method, demonstrating the potential of DP in predicting large-scale complex solid solutions. This work may provide a reference for the subsequent design of ferroelectrics and large-scale simulations.

Methods

Preparation and experimental characterization of ceramic samples

The $Ba_{0.926}Ca_{0.074}Ti0_{.892}Sn_{0.108}O_3$ ceramics were synthesized using a conventional solid-state reaction method with high-purity raw materials: $BaCO_3$, $CaCO_3$, SnO_2, and TiO_2 (AR, Sinopharm Chemical Reagent Co., Ltd., China). The powders were weighed according to the desired composition and mixed in ethanol with zirconia balls for 4 h. The powder mixture was then dried and calcined at 1250 °C for 4 h. After calcination, the powders were crushed and ball-milled for an additional 10 h with 0.5 wt % polyvinyl butyral (PVB) binder. Following drying and sieving, the powder mixture was pressed into disk-shaped samples (10 mm in diameter and 0.7 mm thick) under a pressure of 150–200 MPa. The green pellets were heated to 600 °C to burn off the binder and subsequently sintered at 1450–1550 °C for 3 h in air, with a heating rate of 5 °C/min. The microstructures were characterized using Thermo scientific Talos F200X G2 TEM operated at 200 kV. High Angle Angular Dark Field-Scanning

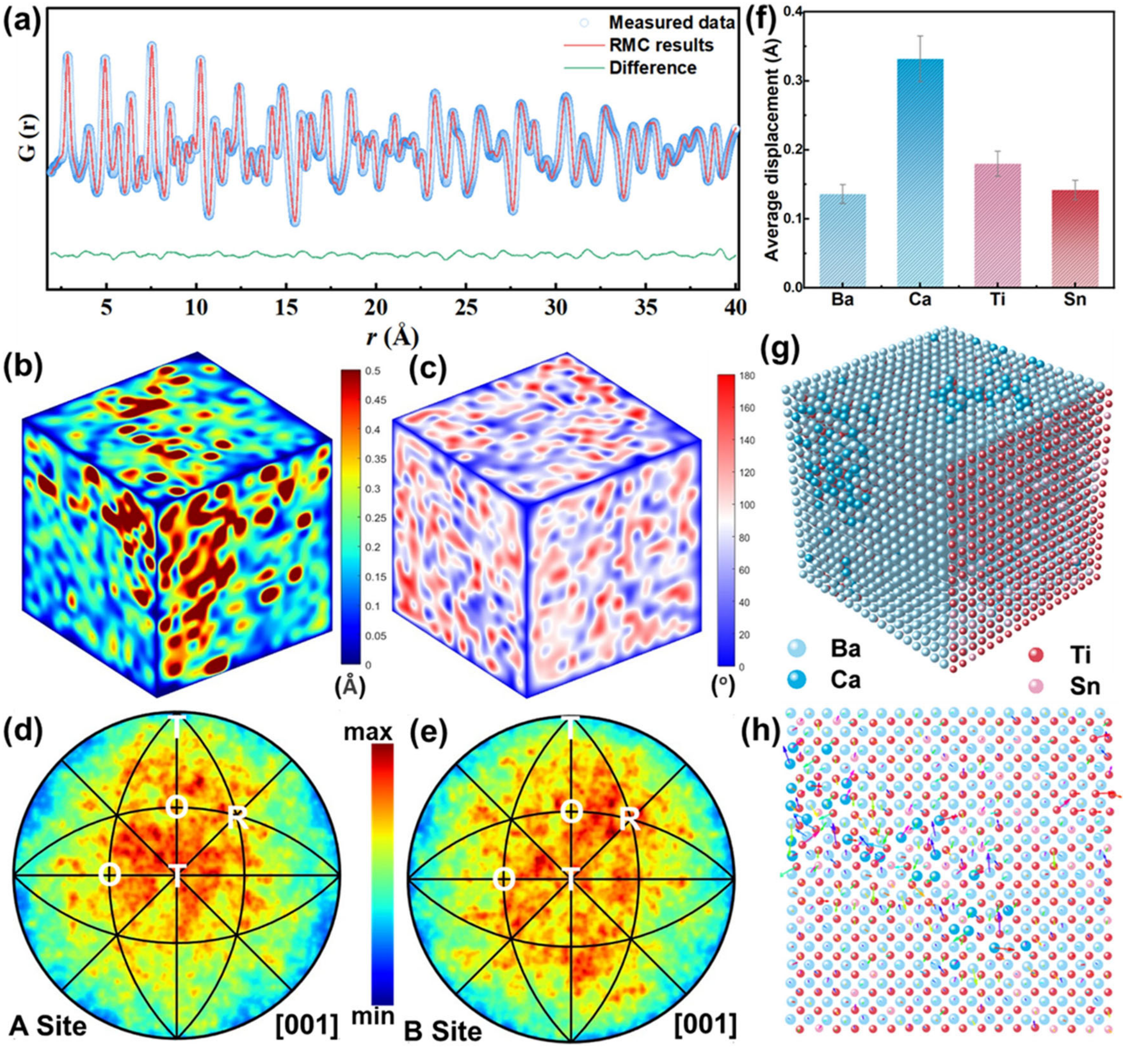

Fig. 8 | The 3D atomic configuration information constructed by fitting neutron-based total scattering data through reverse Monte Carlo (RMC) algorithm. **a** Refinement results of neutron-based pair distribution function (PDF). **b**, **c** 3D distribution of displacement magnitude and polar direction (the angle between the unit-cell polar vector and [001]c direction). **d**, **e** Stereographic projection of A-site and B-site displacements viewing along [001]. **f** Average polar displacement magnitudes of different cations. **g** 3D distribution of different cations, **h** 2D cation distribution and the corresponding polarization mapping in an extracted slice.

Transmission Electron Microscopy (HAADF-STEM) imaging was performed using a Thermo Scientific Spectra 300 Cs-corrected STEM instrument, operated at 300 kV with convergence semi-angle of 25 mrad and HAADF collection semi-angles of 52–200 mrad. All atomic-scale STEM images were Fourier-filtered using a lattice mask to reduce noise. Atomic positions were determined by fitting with 2D Gaussian peaks, and the angles and magnitudes of atomic displacements were calculated using a MATLAB script. Approximately 1.0 g of powder was placed into a quartz capillary to collect neutron total scattering data at 300 K at the Spallation Neutron Source (SNS), Oak Ridge National Laboratory. High-quality data, with a maximum Q value of ~35 Å^{-1}, were obtained. The pair distribution function, G(r), was Fourier-transformed from the corrected total scattering structure factors, S(Q). A 20 × 20 × 20 (~80 × 80 × 80 Å^3) supercell with pseudo-cubic (Pm-3m) symmetry, comprising 40000 atoms with randomly distributed A-site and B-site atoms, was constructed. Reverse Monte Carlo (RMC) simulations were performed utilizing the RMC-Profile software. Both real-space data, G(r), and reciprocal-space data, S(Q), were simultaneously fitted under bond-valence sum and coordination constraints. The 3D distribution of polar displacements, polar vectors, polar projections, and other related quantities were analyzed using custom MATLAB scripts.

DFT calculations

The DFT calculation to build random perturbation structures is used to generate training datasets for DP models. For the 11 solid solution components mentioned above, we use 2 × 2 × 2 supercells containing 40 atoms and $2\sqrt{2} \times 2\sqrt{2} \times 2$ supercells containing 80 atoms, respectively. All calculations use plane-wave basis, Perdew–Burke–Ernzerhof (PBE) exchange correlation functionals under generalized gradient approximation[68,69], all are applied in the Vienna Ab initio Simulation Package software[69,70] with the projector augmented-wave formalism[71,72]. After testing, 10^{-4} eV to be used as the convergency criterion in electric self-consistent step, a cutoff energy of 600 ev and a k-space of 0.20 Å^{-1} are sufficient for energy and force convergence.

The construction of deep-learning potential

In the DP model, the potential surface is described as the sum of the potential energies of each atom $E = \sum E_i$, where E_i represents the potential of the i atom against all atoms around its local environment within the cutoff radius R_c. Because of only a function of coordinates and atomic types, the DP model directly has the characteristic of multi-body potential. Afterwards, it is necessary to construct the input layer (or descriptor) of the ANN through coordinate transformation that preserves rotation and translation symmetry, which could be written as

$$\left\{D_{ij}\right\} = \left\{\frac{1}{R_{ij}}, \frac{x_{ij}}{R_{ij}^2}, \frac{y_{ij}}{R_{ij}^2}, \frac{z_{ij}}{R_{ij}^2}\right\} \tag{4}$$

In order to train an effective ANN, the loss function is defined as

$$L\left(p_\varepsilon, p_f, p_\xi\right) = p_\varepsilon \Delta\varepsilon^2 + \frac{p_f}{3N}\sum_i \left|\Delta F_i\right|^2 + \frac{p_\xi}{9}||\Delta\xi||^2 \tag{5}$$

Among them, Δ reflects the ANN's error between the predicted and true values on the training datasets. ε represents the sum energy to the system, F_i stands for the force collected from the derivative of energy to atomic coordinates: $F_{i,\alpha} = \partial E/\partial R_{i,\alpha}$, and virtual tensor $\xi = -0.5\sum R_i \otimes F_i$, all of the data could be emerged by DFT calculation. Besides p_ε, p_f, p_ξ represents their respective weight coefficients, the higher the weight, the greater the impact of the change to the loss function. Obviously, the loss function measures the performance scale of ANN's error on the training sets, the smaller the absolute value of the loss function, the better manifestation of ANN on the training sets. For ANN, its nodes and several previous nodes connected to it can be described as a function:

$$\widetilde{d}_k = \sigma\left(\sum_i w_{ki} d_i + b_k\right) \tag{6}$$

Among them, σ is the activation function, $\widetilde{d}_k$ is the value of present node meanwhile d_i represent as the previous nodes respectively. w_{ki} represents the weight of the previous node i on the value of node k, the bias factor is b_k. The basic method for training ANN can be summarized as optimizing the weight factor w_{ki} and bias factor b_k of each node through back-propagation algorithm to minimize the loss function. Meanwhile, ANN may not only overfit the training datasets but also fail to accurately reflect the condition of the potential surface. Therefore, four ANN models need to be train with the same training sets but different initial parameters $\left\{w_{ki}, b_k\right\}$, which is the convergence judgment step in this paper. The 3-layer embedding nets and fitting networks are chosen as (25, 50, 100) and (120, 120, 120), respectively.

In this work, the cutoff radius R_c is set as 6.0 Å. The loss function coefficients p_ε and p_ξ increase from 0.02 to 2 and 0.02 to 0.5, on the contrary the force term p_f decreases from 1000 to 2. This indicates that at the beginning of ANN model training, the force term dominates, while towards the end of training, the positions of the three terms tend to be similar. This approach is often considered an effective way to accelerate model convergency, because the output layer of ANN model is the energy of the whole system, that is a holistic behavior. On the contrary the force is generated by the derivative of energy and associates to the atomic coordinates, which can effectively reflect the actual condition of each atom in the system. Therefore, setting the force term as crucial at the beginning is to allow the model to preferentially fit the atomic configuration and layout in the system, avoiding the model deviate significantly from the real situation. On this basis, by fine-tuning the ANN parameters $\left\{w_{ki}, b_k\right\}$, the model can fit energy, force and virtual tensor well near the terminated process. Therefore, the force term is not only applied to evaluate the predictive ability for random structures but also convergency of models.

Usually, we use it as a judgment basis

$$\Delta = \max\sqrt{\left\langle ||F_i - \left\langle F_i\right\rangle||^2\right\rangle} \tag{7}$$

Among them, F_i represents the force term to every structural prediction for each model, while $\left\langle F_i\right\rangle$ represents the average value of the four models to force prediction. Furthermore, we take $\sigma_{high} = 0.5$ and $\sigma_{low} = 0.125$, When all four models have $\Delta < \sigma_{low}$ for random structures, we believe that the model has converged and can fully describe the chemical spatial parameters of the system. Otherwise, we will randomly select several structures within $\sigma_{low} < \Delta < \sigma_{high}$ to perform DFT calculations, and then add them to the training set for the next cycle (see Fig.1 in the main text) until the model fully converges. The above loop management can be implemented in the DeePMD-kit and DPGEN package[26,73].

Molecular dynamics simulation

The MD simulations employed in this work all are adopted with periodic boundary condition and a time step of 2 fs to reflect the motion of atoms, all the processes are achieved in Lammps package[74]. And using isothermal isobaric ensemble (NPT), A Nose Hoover thermostat and Parrinello Rahman barostat respectively were used to control pressure and temperature, that are set as 300 K and 1 kbar to conduct the simulation in this work. In the sample exploration stage, use supercells equivalent to the steps mentioned above in DFT to explore its structure. In subsequent work, a 12 × 12 × 4 supercell containing 2880 atoms was used to measure the component driven phase transition and physical properties of $Ba_{1-y}Ca_yTi_{1-x}Sn_xO_3$ solid solution. Finally, a supercell containing 1536 primitive cells and 7680 atoms was established for comparison with TEM images. The above process is run using a single NVIDIA GeForce RTX 4090 graphics card.

Data availability

The dataset and models for the co-doped BaTiO3 solid solution in this work are available in a public repository: https://www.aissquare.com/datasets/detail?pageType=datasets&name=BaTiO3_MLIP&id=380. Additional data that support the findings of this study are available from the corresponding author on reasonable requests.

Code availability

Codes are openly available in a public repository: https://www.aissquare.com/datasets/detail?pageType=datasets&name=BaTiO3_MLIP&id=380. Additional codes that support the findings of this study are available from the corresponding author on reasonable requests.

Received: 25 July 2025; Accepted: 20 October 2025;

References

1. Jo, W. et al. Giant electric-field-induced strains in lead-free ceramics for actuator applications–status and perspective. *J. Electroceram.* **29**, 71–93 (2012).
2. Zhang, S. et al. Advantages and challenges of relaxor-$PbTiO_3$ ferroelectric crystals for electroacoustic transducers—a review. *Prog. Mater. Sci.* **68**, 1–66 (2015).
3. Zheng, T., Wu, J., Xiao, D. & Zhu, J. Recent development in lead-free perovskite piezoelectric bulk materials. *Prog. Mater. Sci.* **98**, 552–624 (2018).
4. Liu, W. & Ren, X. Large piezoelectric effect in Pb-free ceramics. *Phys. Rev. Lett.* **103**, 257602 (2009).
5. Noheda, B. et al. Tetragonal-to-monoclinic phase transition in a ferroelectric perovskite: the structure of $PbZr_{0.52}Ti_{0.48}O_3$. *Phys. Rev. B* **61**, 8687 (2000).
6. Lv, X., Zhu, J., Xiao, D., Zhang, X. -x. & Wu, J. Emerging new phase boundary in potassium sodium-niobate based ceramics. *Chem. Soc. Rev.* **49**, 671–707 (2020).
7. Wu, J., Xiao, D. & Zhu, J. Potassium–sodium niobate lead-free piezoelectric materials: past, present, and future of phase boundaries. *Chem. Rev.* **115**, 2559–2595 (2015).
8. Sholl, D. S. & Steckel, J. A. *Density Functional Theory: A Practical Introduction* (John Wiley & Sons, 2022).
9. Burke, K. Perspective on density functional theory. *J. Chem. Phys.* **136**, 150901 (2012).

10. Yoshida, S., Akamatsu, H. & Hayashi, K. Electronic origin of non-zone-center phonon condensation: Octahedral rotation as a case study. *Phys. Rev. Lett.* **127**, 215701 (2021).
11. Gu, T. et al. Cooperative couplings between octahedral rotations and ferroelectricity in perovskites and related materials. *Phys. Rev. Lett.* **120**, 197602 (2018).
12. Kim, K., Hwang, W., Oh, S.-H. V. & Soon, A. Exploring anharmonic lattice dynamics and dielectric relations in niobate perovskites from first-principles self-consistent phonon calculations. *npj Comput. Mater.* **9**, 154 (2023).
13. Chen, L.-Q. Phase-field models for microstructure evolution. *Annu. Rev. Mater. Res.* **32**, 113–140 (2002).
14. Chen, L. Q. Phase-field method of phase transitions/domain structures in ferroelectric thin films: a review. *J. Am. Ceram. Soc.* **91**, 1835–1844 (2008).
15. Li, F. et al. The origin of ultrahigh piezoelectricity in relaxor-ferroelectric solid solution crystals. *Nat. Commun.* **7**, 13807 (2016).
16. Li, F., Zhang, S., Xu, Z. & Chen, L. Q. The contributions of polar nanoregions to the dielectric and piezoelectric responses in domain-engineered relaxor-PbTiO$_3$ crystals. *Adv. Funct. Mater.* **27**, 1700310 (2017).
17. Li, T. et al. High-performance strain of lead-free relaxor-ferroelectric piezoceramics by the morphotropic phase boundary modification. *Adv. Funct. Mater.* **32**, 2202307 (2022).
18. Dai, C. et al. Tunable nanoscale evolution and topological phase transitions of a polar vortex supercrystal. *Adv. Mater.* **34**, 2106401 (2022).
19. Liu, Y. et al. Phase-field simulations of tunable polar topologies in lead-free ferroelectric/paraelectric multilayers with ultrahigh energy-storage performance. *Adv. Mater.* **34**, 2108772 (2022).
20. Zhou, L. et al. Order–disorder transitions in a polar vortex lattice. *Adv. Funct. Mater.* **32**, 2111392 (2022).
21. Behera, P. et al. Anisotropic ferroelectricity in polar vortices. *Adv. Mater.* **37**, 2410149 (2025).
22. Hong, Z. et al. Role of point defects in the formation of relaxor ferroelectrics. *Acta Mater.* **225**, 117558 (2022).
23. Zhang, Y.-L. et al. Dislocation-induced giant dielectric and piezoelectric responses in BaTiO$_3$ single crystals by phase-field simulations. *Acta Mater*. **299**, 121469 (2025).
24. LeCun, Y., Bengio, Y. & Hinton, G. Deep learning. *Nature* **521**, 436–444 (2015).
25. Choudhary, K. et al. Recent advances and applications of deep learning methods in materials science. *npj Comput. Mater.* **8**, 59 (2022).
26. Wang, H., Zhang, L. & Han, J. DeePMD-kit: A deep learning package for many-body potential energy representation and molecular dynamics. *Comput. Phys. Commun.* **228**, 178–184 (2018).
27. Zhang, L. et al. Deep potential molecular dynamics: a scalable model with the accuracy of quantum mechanics. *Phys. Rev. Lett.* **120**, 143001 (2018).
28. Zhang, Y., Tiňo, P., Leonardis, A. & Tang, K. A survey on neural network interpretability. *IEEE Trans. Emerg. Top. Comput. Intell.* **5**, 726–742 (2021).
29. Yang, M., Raucci, U. & Parrinello, M. Reactant-induced dynamics of lithium imide surfaces during the ammonia decomposition process. *Nat. Catal.* **6**, 829–836 (2023).
30. Zhang, L., Wang, H., Car, R. & E., W. Phase diagram of a deep potential water model. *Phys. Rev. Lett*. **126**, 236001 (2021).
31. Zhang, X.-W. et al. Polarization-driven band topology evolution in twisted MoTe$_2$ and WSe$_2$. *Nat. Commun.* **15**, 4223 (2024).
32. Ma, L. et al. Ultrahigh oxygen ion mobility in ferroelectric hafnia. *Phys. Rev. Lett.* **131**, 256801 (2023).
33. Bai, L. et al. Intrinsic ferroelectric switching in two-dimensional α-In$_2$Se$_3$. *ACS Nano* **18**, 26103–26114 (2024).
34. Ying, P., Natan, A., Hod, O. & Urbakh, M. Effect of interlayer bonding on superlubric sliding of graphene contacts: a machine-learning potential study. *ACS Nano* **18**, 10133–10141 (2024).
35. Fan, D., Naskar, S. & Maurin, G. Unconventional mechanical and thermal behaviours of MOF CALF-20. *Nat. Commun.* **15**, 3251 (2024).
36. Che, J., Huang, W., Ren, G., Linghu, J. & Wang, X. Dual-channel phonon transport leads to low thermal conductivity in pyrochlore La$_2$Hf$_2$O$_7$. *Ceram. Int.* **50**, 22865–22873 (2024).
37. Wu, J. et al. Deep-potential enabled multiscale simulation of gallium nitride devices on boron arsenide cooling substrates. *Nat. Commun.* **15**, 2540 (2024).
38. Zhao, K. et al. Octahedral tilt distortion in negative thermal expansion in the fluorides CaZrF$_6$ and ScF$_3$. *Phys. Rev. B* **110**, 064322 (2024).
39. Saito, Y. et al. Lead-free piezoceramics. *Nature* **432**, 84–87 (2004).
40. Wang, D. et al. Ultrahigh piezoelectricity in lead-free piezoceramics by synergistic design. *Nano Energy* **76**, 104944 (2020).
41. Zhao, C. et al. Practical high piezoelectricity in barium titanate ceramics utilizing multiphase convergence with broad structural flexibility. *J. Am. Chem. Soc.* **140**, 15252–15260 (2018).
42. Fu, J., Xie, A., Li, T. & Zuo, R. Ultrahigh piezoelectricity in (Ba, Ca)(Ti, Sn)O$_3$ lead-free compounds with enormous domain wall contribution. *Acta Mater.* **230**, 117862 (2022).
43. Tao, H. et al. Ultrahigh performance in lead-free piezoceramics utilizing a relaxor slush polar state with multiphase coexistence. *J. Am. Chem. Soc.* **141**, 13987–13994 (2019).
44. Takenaka, H., Grinberg, I., Liu, S. & Rappe, A. M. Slush-like polar structures in single-crystal relaxors. *Nature* **546**, 391–395 (2017).
45. Cheng, Z.-Y., Katiyar, R., Yao, X. & Bhalla, A. Temperature dependence of the dielectric constant of relaxor ferroelectrics. *Phys. Rev. B* **57**, 8166 (1998).
46. Ponomareva, I. & Bellaiche, L. Nature of dynamical coupling between polarization and strain in nanoscale ferroelectrics from first principles. *Phys. Rev. Lett.* **101**, 197602 (2008).
47. Lei, C., Bokov, A. A. & Ye, Z.-G. Ferroelectric to relaxor crossover and dielectric phase diagram in the BaTiO$_3$–BaSnO$_3$ system. *J. Appl. Phys*. **101**, 084105 (2007).
48. Surampalli, A., Egli, R., Prajapat, D., Meneghini, C. & Reddy, V. R. Reentrant phenomenon in the diffuse ferroelectric BaSn$_{0.15}$Ti$_{0.85}$O$_3$: local structural insights and first-order reversal curves study. *Phys. Rev. B* **104**, 184114 (2021).
49. Cohen, R. & Krakauer, H. Lattice dynamics and origin of ferroelectricity in BaTiO$_3$: linearized-augmented-plane-wave total-energy calculations. *Phys. Rev. B* **42**, 6416 (1990).
50. Cohen, R. E. Origin of ferroelectricity in perovskite oxides. *Nature* **358**, 136–138 (1992).
51. Vendik, O. G. & Zubko, S. P. Modeling the dielectric response of incipient ferroelectrics. *J. Appl. Phys.* **82**, 4475–4483 (1997).
52. Sokolović, I., Schmid, M., Diebold, U. & Setvin, M. Incipient ferroelectricity: a route towards bulk-terminated SrTiO$_3$. *Phys. Rev. Mater.* **3**, 034407 (2019).
53. Lemanov, V., Sotnikov, A., Smirnova, E., Weihnacht, M. & Kunze, R. Perovskite CaTiO$_3$ as an incipient ferroelectric. *Solid State Commun.* **110**, 611–614 (1999).
54. Lemanov, V. Phase tansitions and dielectric relaxation in incipient ferroelectrics with the perovskite structure. *Ferroelectrics* **346**, 97–109 (2007).
55. Haeni, J. et al. Room-temperature ferroelectricity in strained SrTiO$_3$. *Nature* **430**, 758–761 (2004).
56. Pertsev, N., Tagantsev, A. & Setter, N. Phase transitions and strain-induced ferroelectricity in SrTiO$_3$ epitaxial thin films. *Phys. Rev. B* **61**, R825 (2000).
57. He, R. et al. Structural phase transitions in SrTiO$_3$ from deep potential molecular dynamics. *Phys. Rev. B* **105**, 064104 (2022).

58. Aschauer, U. & Spaldin, N. A. Competition and cooperation between antiferrodistortive and ferroelectric instabilities in the model perovskite $SrTiO_3$. *J. Phys. Condens. Matter* **26**, 122203 (2014).
59. Viana, R., Lunkenheimer, P., Hemberger, J., Böhmer, R. & Loidl, A. Dielectric spectroscopy in $SrTiO_3$. *Phys. Rev. B* **50**, 601 (1994).
60. Kvyatkovskii, O. Quantum effects in incipient and low-temperature ferroelectrics (a review). *Phys. Solid State* **43**, 1401–1419 (2001).
61. Samara, G., Sakudo, T. & Yoshimitsu, K. Important generalization concerning the role of competing forces in displacive phase transitions. *Phys. Rev. Lett.* **35**, 1767 (1975).
62. Rondinelli, J. M., Eidelson, A. S. & Spaldin, N. A. Non-d_0 Mn-driven ferroelectricity in antiferromagnetic $BaMnO_3$. *Phys. Rev. B* **79**, 205119 (2009).
63. Guo, J. et al. Strain-induced ferroelectricity and spin-lattice coupling in $SrMnO_3$ thin films. *Phys. Rev. B* **97**, 235135 (2018).
64. Bersuker, I. B. Pseudo-Jahn–Teller Effect–a two-state paradigm in formation, deformation, and transformation of molecular systems and solids. *Chem. Rev.* **113**, 1351–1390 (2013).
65. Nagai, T., Mochizuki, Y., Yoshida, S. & Kimura, T. Chemical aspect of displacive-type ferroaxial phase transition from perspective of second-order Jahn–Teller effect: NASICON systems as an example. *J. Am. Chem. Soc.* **145**, 8090–8098 (2023).
66. Koiso, H. et al. Thermal expansion and phase stability of BF_3 (B= Sc, Y, La, Al, Ga, In) from first principles. *Phys. Rev. B* **110**, 064104 (2024).
67. Levin, I., Krayzman, V. & Woicik, J. C. Local-structure origins of the sustained Curie temperature in (Ba, Ca)TiO_3 ferroelectrics. *Appl. Phys. Lett*. **102**, 162906 (2013).
68. Perdew, J. P., Burke, K. & Ernzerhof, M. Generalized gradient approximation made simple. *Phys. Rev. Lett.* **77**, 3865 (1996).
69. Kresse, G. & Furthmüller, J. Efficiency of ab-initio total energy calculations for metals and semiconductors using a plane-wave basis set. *Comput. Mater. Sci.* **6**, 15–50 (1996).
70. Kresse, G. & Furthmüller, J. Efficient iterative schemes for ab initio total-energy calculations using a plane-wave basis set. *Phys. Rev. B* **54**, 11169 (1996).
71. Blöchl, P. E. Projector augmented-wave method. *Phys. Rev. B* **50**, 17953 (1994).
72. Kresse, G. & Joubert, D. From ultrasoft pseudopotentials to the projector augmented-wave method. *Phys. Rev. B* **59**, 1758 (1999).
73. Zhang, Y. et al. DP-GEN: A concurrent learning platform for the generation of reliable deep learning based potential energy models. *Comput. Phys. Commun.* **253**, 107206 (2020).
74. Dickey, J. & Paskin, A. Computer simulation of the lattice dynamics of solids. *Phys. Rev.* **188**, 1407 (1969).

Acknowledgements

This work was supported by the National Key R&D Program of China (Grant No. 2023YFB3508200), the Outstanding Young Scientist Program of Beijing Colleges and Universities (JWZQ20240101015), and the National Natural Science Foundation of China (Grant Nos. 92370104, 22235002 and 52172181). We acknowledge the computational resource from Beijing PARATERA Tech Corp, LTD.

Author contributions

X.M. and S.L. conceived the idea and designed the project. X.M. wrote the initial draft. H.Q., S.L. and J.C. revised the paper. S.L., H.Q. and J.C. provided relevant funds. H.Q., J.F., L.F., and J.W. completed the experimental design and verification. All authors reviewed and edited the manuscript. X.M., J.F., and L.F. contributed equally to this work.

Competing interests

The authors declare no competing interests.

Additional information

Supplementary information The online version contains supplementary material available at https://doi.org/10.1038/s41524-025-01847-4.

Correspondence and requests for materials should be addressed to He Qi, Shi Liu or Jun Chen.